Langmuir

Article

pubs.acs.org/Langmuir

Electrocatalytic Oxygen Evolution over Supported Small Amorphous Ni–Fe Nanoparticles in Alkaline Electrolyte

Yang Qiu, Le Xin, and Wenzhen Li*

Department of Chemical Engineering, Michigan Technological University, Houghton, Michigan 49931, United States

ABSTRACT: The electrocatalytic oxygen evolution reaction (OER) is a critical anode reaction often coupled with electron or photoelectron CO_2 reduction and H_2 evolution reactions at the cathode for renewable energy conversion and storage. However, the sluggish OER kinetics and the utilization of precious metal catalysts are key obstacles in the broad deployment of these energy technologies. Herein, inexpensive supported 4 nm Ni–Fe nanoparticles ($Ni_yFe_{1-y}O_x/C$) featuring amorphous structures have been prepared via a solution-phase nanocapsule method for active and durable OER electrocatalysts in alkaline electrolyte. The Ni–Fe nanoparticle catalyst containing 31% Fe ($Ni_{0.69}Fe_{0.31}O_x/C$) shows the highest activity, exhibiting a 280 mV overpotential at 10 mA cm^{-2} (equivalent to 10% efficiency of solar-to-fuel conversion) and a Tafel slope of 30 mV dec^{-1} in 1.0 M KOH solution. The achieved OER activity outperforms NiO_x/C and commercial Ir/C catalysts and is close to the highest performance of crystalline Ni–Fe thin films reported in the literature. In addition, a Faradaic efficiency of 97% measured on $Ni_{0.69}Fe_{0.31}O_x/C$ suggests that carbon support corrosion and further oxidation of nanoparticle catalysts are negligible during the electrocatalytic OER tests. $Ni_{0.69}Fe_{0.31}O_x/C$ further demonstrates high stability as there is no apparent OER activity loss (based on a chronoamperometry test) or particle aggregation (based on TEM image observation) after a 6 h anodization test. The high efficiency and durability make these supported amorphous Ni–Fe nanoparticles potentially applicable in the (photo)electrochemical cells for water splitting to make H_2 fuel or CO_2 reduction to produce usable fuels and chemicals.

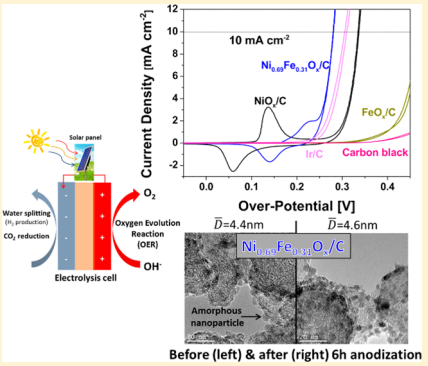

1. INTRODUCTION

As global energy demand is increasing rapidly, intensive research and development have been devoted to novel technologies for the conversion and storage of sustainable energy sources, such as water splitting to H_2 fuel, CO_2 reduction to fuels, and biomass upgrading to biofuels.[1−8] However, the electrocatalytic oxygen evolution reaction (OER, $2H_2O \leftrightarrow 4H^+ + O_2 + 4e^-$ in acidic media or $4OH^- \leftrightarrow 2H_2O + O_2 + 4e^-$ in basic media) often coupled with these processes at the anode is a slow reaction that requires an overpotential in substantial excess of its thermodynamic potential (1.23 V vs RHE, at standard temperature and pressure) to deliver an acceptable current density, e.g., 10 mA cm^{-2} (based on a 10% solar-to-fuel conversion efficiency).[9−12] Many research efforts have been intensively focused on this reaction, targeting to seek more efficient OER electrocatalysts at lower overpotential to reduce the input energy cost.[6,11,13] IrO_2 and RuO_2 have been identified as the most active catalysts for OER; however, the scarcity and high cost of these precious metals make them undesirable for widespread applications.[2,6,14] Therefore, exploring efficient and durable catalysts based on earth-abundant metals has been the focal point of current research. Although various first-row transition monometal oxides, such as CoO_x and MnO_x with different structures, were synthesized and exhibited promising activity toward OER,[15−20] they still underperformed with respect to IrO_2 and RuO_2 due to the strength of the M–O (M=Co, Mn, etc.) bond when their specific defect was too strong or too weak.[21] Therefore, more multicomponent complex catalysts have been studied.[22−24] For example, Suntivich et al. have demonstrated intrinsic OER activity on a series of perovskite oxides through plotting a volcano-shaped graph and found that $Ba_{0.5}Sr_{0.5}Co_{0.8}Fe_{0.2}O_{3-\delta}$ (BSCF) exhibited the highest activity for OER.[25] However, the large particle size (~200 nm) of perovskite oxides leads to quite small surface areas, thus limiting further mass activity enhancement. Recently, the Ni–Fe bimetallic system has been investigated and was found to be able to serve as an efficient OER catalyst.[26−28] Dai and coworkers successfully prepared a Ni–Fe-layered double-hydroxide multiwalled carbon nanotube (MWCNT) complex with an average size of 50 nm via a hydrothermal synthesis method. They proposed that Fe^{3+} replaces Ni^{2+} in the crystalline α-$Ni(OH)_2$ of the layered double-hydroxide structure, which results in a high activity of OER.[29] Corrigan et al. electrodeposited iron impurity in a nickel oxide thin film and found that the directly incorporated iron can also increase the OER activity of the Ni film catalyst.[30,31] Subsequently, a variety of Ni–Fe-based catalysts with thin-film geometry were prepared, such as an evaporation-induced self-assembly (EISA) Ni–Fe oxide thin film by Grosso et al.[32] Landon et al. reported that in NiO and Fe_2O_3 a thin-film structure coexisted and crystalline $NiFe_2O_4$ could be a contributing phase to enhanced OER activity.[26] On

Received: April 1, 2014
Revised: June 7, 2014
Published: June 10, 2014

   dx.doi.org/10.1021/la501246e | *Langmuir* 2014, 30, 7893−7901

the other hand, Bell et al. used in situ Raman spectroscopy to demonstrate the oxidation states of Ni and Fe as well as the corresponding structure of Fe in the Ni−Fe thin film. The results also implied that the presence of Fe can promote OER activity in the NiO_x film without the observation of any crystalline $NiFe_2O_4$.[33] It has been well recognized that the catalyst surface area will strongly influence the mass activity of catalysts. A nanoparticle catalyst with a smaller size can provide more active sites on which to achieve a higher OER activity on a mass basis.[16,34] In addition, catalysts with smaller nanoscale dimensions and higher OER activity can be readily fabricated into practical electrochemical cells. However, few studies so far have been focused on small Ni−Fe nanoparticles as an OER electrocatalyst.

Herein, we present the synthesis of 4 nm amorphous Ni−Fe nanoparticles supported on XC-72 carbon black via a modified organic solution phase reduction method. Low crystallinity in NiO_x or FeO_x nanoparticles was characterized by XRD and TEM-SAED. The amorphous Ni−Fe structure has shown surprisingly high OER activity in alkaline media, which outperforms most Ni−Fe thin films previously reported and a commercial carbon-supported Ir nanoparticle catalyst. Moreover, the high stability and Faradaic efficiency of OER achieved on the amorphous Ni−Fe nanoparticle catalysts suggest promising opportunities for practical sustainable energy conversion and storage applications in the future.

2. EXPERIMENTAL SECTION

2.1. Preparation of Carbon-Supported Ni−Fe Nanoparticles. All carbon-black-supported Ni−Fe nanoparticle catalysts were prepared through a modified organic solution phase nanocapsule approach, which has been reported elsewhere.[35−37] The brief synthesis procedure for the Ni−Fe catalysts with a metal loading of ca. 20 wt % is described as follows. $Ni(acac)_2$ (Aldrich Chemistry, 95%), $Fe(acac)_2$ (Aldrich Chemistry, 99.95%), and Vulcan XC-72 carbon black (FuelCell Store) were mixed in 25 mL of benzyl ether (Alfa Aesar, 98%). The stoichiometry of each metal precursor was varied based on the targeting ratios of Ni to Fe. Note that the Fe precursor was added in 200% excess of the stoichiometric amount because Fe^{2+} could not be completely reduced under the synthesis conditions (e.g., for the synthesis of $Ni_{0.5}Fe_{0.5}O_x$/C, 0.25 mmol $Ni(acac)_2$ + 0.25 × 3 mmol $Fe(acac)_2$ was used). Then, the mixed solution was heated to 60 °C under nitrogen flow, and the surfactants (oleylamine OAM (Aldrich Chemistry, 70%), oleic acid OAc (Aldrich Chemistry, 95%)) were added to the system, followed by maintaining for 5 min to ensure the complete dissolution of precursors and surfactants. As the temperature was further increased to 120 °C, $LiBEt_3H$ (1.0 M in THF, Acros Organics) was quickly injected and held for 30 min. Then, the temperature was rapidly ramped to 180 °C and held for an additional 1 h. The carbon-supported Ni−Fe catalysts were finally collected after filtration, washing with copious ethanol (Pharmco-Aaper, 200 proof), and drying in a vacuum oven at 50 °C for 24 h.

2.2. Physical Characterization. The metal loading and composition of the catalyst were analyzed by inductively coupled plasma optical emission spectroscopy (ICP-OES Optima 7000 DV, PerkinElmer). The specimen was prepared by dissolving 10 mg of catalyst in 4 mL of fresh aqua regia, followed by diluting to 250 mL with deionized water (18.2 MΩ). The catalyst crystallinity was characterized by using a Scintag XDS-2000 θ/θ diffractometer with Cu Kα radiation (λ = 1.5406 Å), with a tube current of 35 mA and a tube voltage of 45 kV. Transmission electron microscopy (JEOL JEM-2010) was utilized to determine the catalyst morphology, size, and diffraction pattern with an operation voltage of 200 kV.

2.3. Electrochemical Characterization and OER Tests. Electrochemical characterizations and tests were performed in an electrochemical cell (AFCELL3, Pine Instrument). A rotating disk electrode (RDE) and rotating ring disk electrode (RRDE) were used for the examination of OER kinetics without the interference of mass-transfer effects and for the analysis of the OER Faradaic efficiency, respectively. A coiled platinum counter electrode, which was isolated by a fritted glass tube from the main test electrolyte, and a Hg/HgO (MMO) reference electrode with 1.0 M KOH filling solution were used throughout the electrochemical characterizations. The 1.0 M KOH electrolytes prepared from bioxtra grade (Macron, 86%) and semiconductor grade (Aldrich Chemistry, 99.99%) reagents was used to test the OER activity and Faradaic efficiency of Ni−Fe electrocatalysts, respectively. A 2.0 mg mL^{-1} solution of catalyst ink was prepared by dispersing carbon-supported Ni−Fe nanoparticles in isopropanol, followed by ultrasonication until no aggregation was visible. The catalyst ink (15 μL) was then dropped onto the surface of a glassy carbon electrode with a 5 mm diameter, and 10 μL of a 0.05 wt % diluted Nafion solution (Ion Power, Inc., 5 wt %, 1100EW) was finally added to the top to fix the catalyst particles.

The standard electrode potential of Hg/HgO/1.0 M KOH (MMO) was 0.098 V vs standard hydrogen electrode (SHE) based on the manufacturer's specification. Then, the potential of the Hg/HgO/1.0 M KOH reference electrode was calculated to be 0.924 V vs the reversible hydrogen electrode (RHE) at pH 14. Thus, the reversible potential of water oxidation, 1.23 V vs RHE at pH 14, could be calculated as 0.306 V vs MMO at pH 14 (1.230−0.924 V = 0.306 V). And the overpotential η was calculated using following equation

$$\eta = E_{\text{applied}} - E_{\text{rev}} - R_{\text{u}} \times i \tag{1}$$

where E_{applied} is the applied potential vs MMO in 1.0 M KOH, R_{u} is the compensated resistance, i is the measured current, and E_{rev} is the reversible potential of OER vs MMO (0.306 V vsMMO at pH 14). The compensated resistance, R_{u}, between working and reference electrodes was determined to be ∼15 Ω in 1.0 M KOH electrolyte by a single-point high-frequency impedance method at 300 mV overpotential, and all of the potentials reported were IR-compensated to 85%.[6,29] All experimental results for the OER activity on Ni−Fe catalysts were reported as current density vs iR corrected applied potential (vs MMO) and overpotential. The current densities are normalized by using geometric surface areas.

2.3.1. Cyclic Voltammetry. The OER activity of Ni−Fe catalysts was determined using cyclic voltammetry (CV). The 1.0 M KOH electrolyte was deaerated by pure oxygen gas for 30 min prior to each experiment. Surfactant removal was first carried out by scanning from −0.8 to 0.65 V (vs MMO) at a 1000 mV s^{-1} scan rate for 50 cycles, followed by catalyst activation in a potential range of 0 to 0.65 V (vs MMO) at a scan rate of 50 mV s^{-1} for 10 cycles. The polarization curves were subsequently obtained using a scan rate of 5 mV s^{-1} between 0 and 0.8 V (vs MMO).

2.3.2. Calculation of the Turnover Frequency (TOF). The TOF is defined per the total number of metal atoms including subsurface metal per second, and the equation is shown as follows, which has been widely used in previous work,[3,6,10,16,33]

$$\text{TOF} = \frac{I}{4 \times F \times m} \tag{2}$$

where I is the measured current at a certain overpotential, F is the Faraday constant with a value of 96 485 C mol^{-1}, and m is the number of moles of the total active metals drop-cast on the glassy carbon electrode.

This TOF is estimated by assuming all of the active metal atoms in the catalysts drop-cast on the glassy carbon electrode are catalytically active for OER. However, this is a gross underestimate of the real TOF, which should be the lower bound, TOF_{min}, because the porous structure of carbon supporting materials could inhibit the perfect connection between the electrolyte and catalysts and some of the subsurface active material atoms might not be accessible for catalyzing the OER.[3,10,16,33]

2.3.3. Faradaic Efficiency. The RRDE was employed to measure the OER Faradaic efficiency over the Ni−Fe catalysts with different compositions. The collection efficiency, N, of RRDE was determined by the current ratio between the ring and disk in 0.01 M $K_3Fe(CN)_6$ +

dx.doi.org/10.1021/la501246e | Langmuir 2014, 30, 7893−7901

Table 1. Summary of Actual Ni−Fe Composition and Average Particle Sizes of $Ni_yFe_{1-y}O_x$/C Catalysts

target Ni/Fe composition	1:0	0.8:0.2	0.7:0.3	0.5:0.5	0.3:0.7	0:1
actual Ni/Fe composition	1:0	0.83:0.17	0.69:0.31	0.46:0.54	0.25:0.75	0:1
average particle size/nm	3.7	4.1	4.4	4.4	4.2	3.4

0.1 M KOH electrolyte, which was 23 ± 1%.[38] This result agrees well with the 25% collected efficiency calculated according to the geometry of RRDE. Pure nitrogen gas flowed into 1.0 M KOH electrolyte prior to each test for 30 min and remained throughout the electrochemical experiments to purge the system. Because of the low magnitude of the ring current, the Pt ring was polished with a diamond slurry (1 μm MetaDi Supreme) before ring current collection in order to minimize the interference of the contaminants. Five microliters of the 1 mg mL^{-1} catalyst ink was dropped onto the surface of the disk electrode, followed by adding 3 μL of diluted Nafion solution (0.05 wt %) to the top. To determine the background current of the ring electrode, the open circuit potential of OER was applied to the disk electrode where no Faradaic reaction occurs, while the Pt ring electrode was held at −0.6 V vs MMO. The background ring current determined was typically lower than 50 μA. Then, the applied voltage was held at several potentials in the OER kinetic-limited region for 1 min. Meanwhile, the ring current was collected under −0.6 V vs MMO.

3. RESULTS AND DISCUSSION

3.1. Catalyst Preparation. The carbon-supported amorphous Ni−Fe nanoparticles ($Ni_yFe_{1-y}O_x$/C) were prepared via a modified solution-phase nanocapsule method. The composition of Ni−Fe nanoparticles was controlled by varying the ratio of two precursors $(Ni(acac)_2$ and $Fe(acac)_2)$. $Fe(acac)_2$ in 200% excess was added in order to achieve the setting ratio and loading of Ni−Fe nanoparticles on the carbon black. Excess Fe precursor was found to be necessary because Fe^{2+} could not be completely reduced under the synthesis conditions, which may be attributed to the more negative redox potential of Fe^{2+}/Fe (−0.440 V vs SHE) compared to that of noble metal catalysts such as Pt^{2+}/Pt (1.200 V vs SHE), Pd^{2+}/Pd (0.987 V vs SHE), and Au^{3+}/Au (1.498 V vs SHE). In addition, in contrast to noble metals, non-noble metals may have a relatively weak bonding strength with the surfactants (oleylamine and oleic acid), leading to poor control over the particle size, morphology, and final composition of catalysts.[35] Through modifying the synthesis conditions, such as the molar ratio of precursors, temperature increase rate, and duration of synthesis, the Fe precursor present in 200% excess was found to be the optimum stoichiometry to ensure that the obtained molar ratios of Ni and Fe approach the setting compositions and metal loadings on the carbon black supporting materials, as confirmed by ICP-OES.

To obtain the amorphous structure of Ni−Fe nanoparticles, postheat treatment was not performed. Nanoparticle aggregation, which often occurs at high temperatures and can lead to a significant decrease in the catalyst surface area and active sites, was minimized under such mild synthesis conditions of the nanocapsule method.[36]

On the other hand, the surfactants may bond at the metal surface, resulting in a blocking for catalytic active sites, which can strongly affect the oxygen evolution reaction (OER) performance of Ni−Fe catalysts. Therefore, copious ethanol was used to wash the catalysts, which has been found to enable surfactant removal to <5 wt % of the final catalyst content.[36] In order to further minimize the interference of surfactant possibly presented after ethanol washing, a cyclic voltammetry scan with 1 V s^{-1} scan rate was performed until the anodic wave become stabilized before obtaining the OER activity over the Ni−Fe electrocatalyst.

3.2. Physical Characterization. The metal loadings (Ni + Fe) of all catalysts were calculated through the total weights of Ni and Fe detected by ICP-OES divided by the total weight of $Ni_yFe_{1-y}O_x$/C determined by weight balance, as shown in the following equation:

$$\frac{(\text{wt of Ni})_{\text{determined by ICP-OES}} + (\text{wt of Fe})_{\text{determined by ICP-OES}}}{\left(\text{total wt of } Ni_yFe_{1-y}O_x/C\right)_{\text{determined by balance}}} = \text{metal loading} \quad (3)$$

Because of the existence of small amounts of surfactant on the surfaces of as-prepared catalysts and the formation of FeO_x and NiO_x as the sample is exposed to air, the metal loading (Ni + Fe) of all of the catalysts has been found to be ∼15 wt %, which is lower than the setting loading of 20 wt % for all of the samples.[39] The metal compositions of as-prepared Ni−Fe catalysts were also obtained by ICP-OES, as shown in Table 1, and the Ni/Fe molar ratio varied from 0.83:0.17 to 0.25:0.75.

XRD was employed to characterize the crystallinity of supported Ni−Fe nanoparticles by scanning from 10 to 100°, and the patterns are shown in Figure 1 and compared to

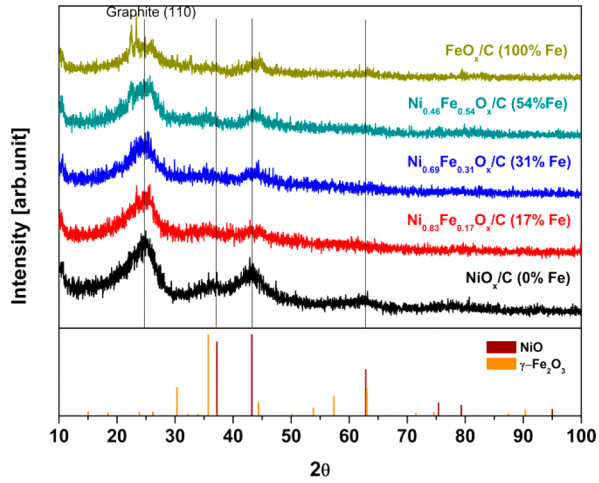

Figure 1. XRD patterns of as-prepared carbon-supported NiO_x, FeO_x, and $Ni_yFe_{1-y}O_x$ nanoparticles with different Fe content. Patterns of NiO [Joint Committee on Powder Diffraction (JCPDS) card 04-0835] and γ-Fe_2O_3 (JCPDS card 39-1346) standards are shown at the bottom.

polycrystalline NiO (Joint Committee on Powder Diffraction JCPDS card 04-0835) and γ-Fe_2O_3 (JCPDS card 39-1346) standards.A low intensity for all characteristic crystalline diffraction peaks was observed, except for the peak related to the graphite (002) facet at ∼25°, which suggests that the NiO_x, FeO_x, and $Ni_yFe_{1-y}O_x$ nanoparticles predominantly feature amorphous structures. For NiO_x/C, only three weak peaks at 37.3, 43.3, and 62.9° were exhibited, representing the NiO (111), (200), and (220) facets, respectively. With increasing Fe content, the characteristic peaks of the γ-Fe_2O_3 (311) and (400) facet at 35.6 and 44.2° were displayed, while the

dx.doi.org/10.1021/la501246e | Langmuir 2014, 30, 7893−7901

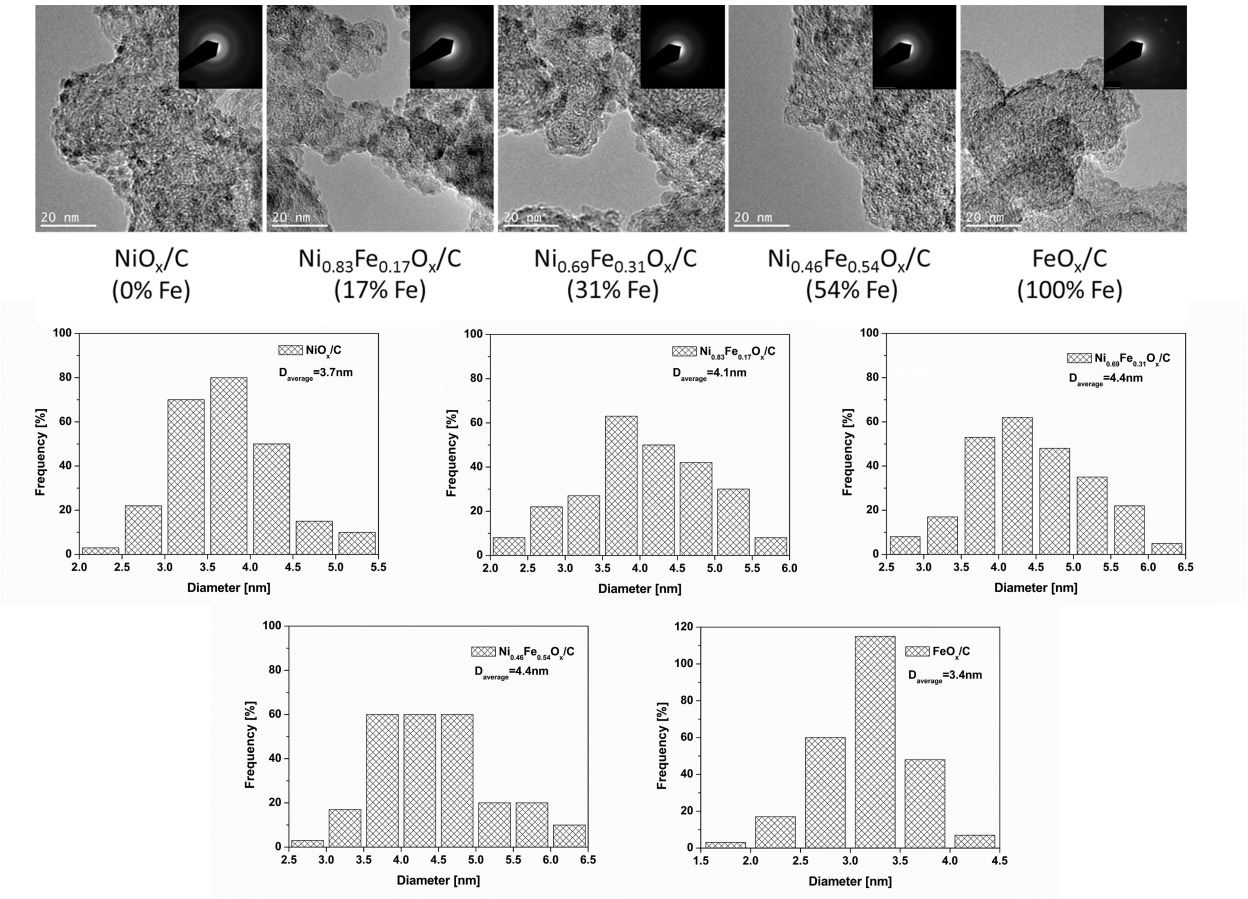

Figure 2. TEM images, corresponding selected-area electron diffraction (SAED) patterns, and particle diameter histograms of carbon-supported NiO_x, FeO_x, and $Ni_yFe_{1-y}O_x$ nanoparticles.

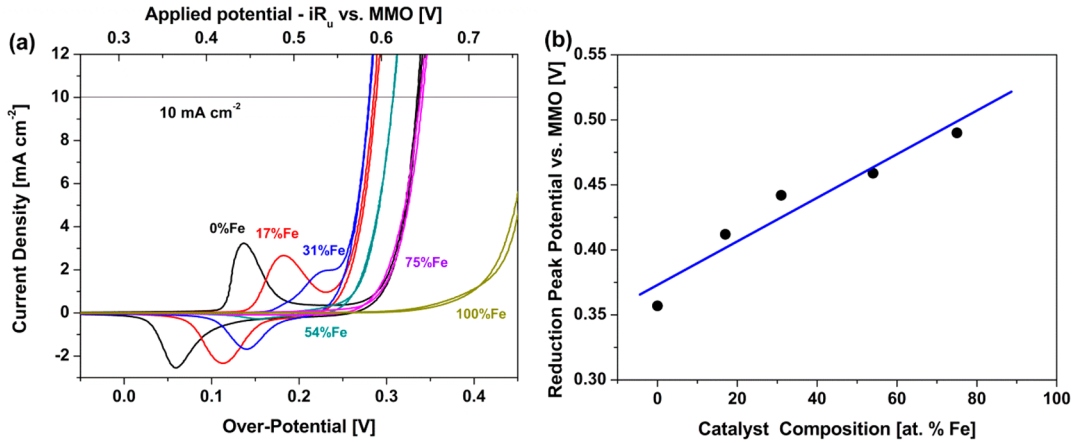

Figure 3. (a) Cyclic voltammograms of carbon-supported NiO_x, FeO_x, and $Ni_yFe_{1-y}O_x$ nanoparticles collected at 5 mV s^{-1} and 1600 rpm in O_2-saturated 1.0 M KOH. (b) Reduction peak potential as a function of Fe content. The line demonstrates a linear fit to the data.

characteristic NiO diffraction peaks gradually disappeared. The two small, sharp peaks at 23.2 and 25.8° are observed on FeO_x/C, which are probably assigned to the diffraction peaks of the γ-Fe_2O_3 (210) and (211) facets. By analyzing all characteristic peaks in the XRD patterns, it may be concluded that small amounts of γ-Fe_2O_3 with low crystallinity are contained in the predominantly amorphous phase in FeO_x and $Ni_yFe_{1-y}O_x$ nanoparticles.[40] However, due to the low intensity and close position of NiO and γ-Fe_2O_3 standard diffraction peaks, the XRD patterns could not reveal the exact crystalline phase in the low-crystalline Ni−Fe nanoparticles. In addition, the XRD patterns provided no evidence for alloyed $NiFeO_x$ and $NiFe_2O_x$ crystals. Therefore, it further confirms that the hypothesized crystalline phases in Ni−Fe nanoparticles are γ-Fe_2O_3 rather than alloyed nickel iron oxides and that the Ni−Fe catalysts are predominantly amorphous.[41] After comparing a variety of standard crystalline Fe oxides (e.g., α-Fe_2O_3, γ-Fe_2O_3, and Fe_3O_4), only the standard XRD pattern of γ-Fe_2O_3 is shown as the major crystalline phase in Figure 1.[40−43]

dx.doi.org/10.1021/la501246e | Langmuir 2014, 30, 7893−7901

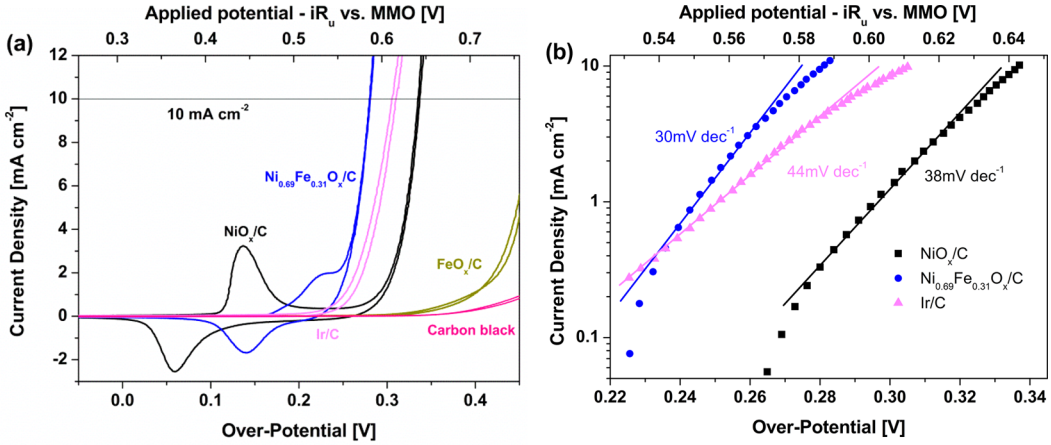

Figure 4. (a) Cyclic voltammograms of carbon-supported NiO_x, FeO_x, $Ni_{0.69}Fe_{0.31}O_x$, Ir nanoparticles, and carbon black. (b) Tafel plots of carbon-supported Ir, NiO_x, and $Ni_{0.69}Fe_{0.31}O_x$ nanoparticles collected at 5 mV s^{-1} and 1600 rpm in O_2-saturated 1.0 M KOH.

TEM images were used to observe the Ni−Fe particle size and size distribution directly, and selected-area electron diffraction (SAED) patterns were employed to investigate the amorphous structure of the Ni−Fe catalysts. From the TEM images and corresponding histograms, all Ni−Fe catalysts were found to be uniform nanoparticles with good dispersion and a narrow size distribution (from 2.0 to 6.5 nm), centered at ca. 4 nm based on the counting of 250 randomly chosen particles over an arbitrarily chosen area, as shown in Figure 2. The average Ni−Fe nanoparticle diameters obtained from TEM are summarized in Table 1. In addition, if highly crystalline nickel, iron oxides, or Ni−Fe alloy is present, then one would expect either a matrix of sharp, bright rings in the TEM-SAED patterns as shown in Figure 2. However, only blurred rings were observed, indicating a predominantly amorphous structure for the as-prepared Ni−Fe catalysts, which is consistent with XRD patterns. Some nearly unnoticeable bright spots with blurred circles were displayed in FeO_x/C, indicating that small amounts of low-crystallinity Fe oxides were contained in the amorphous phase.

3.3. Electrochemical Characterization. *3.3.1. Cyclic Voltammetry of OER.* The cyclic voltammograms of carbon-supported amorphous Ni−Fe catalysts are shown in Figure 3a. In 1.0 M KOH electrolyte, the NiO_x/C and FeO_x/C catalysts exhibited significant differences in both characteristic redox peaks and OER activity. The NiO_x/C displayed redox peaks at overpotentials of 52 and 140 mV (0.358 and 0.446V vs MMO) during the anodic and cathodic scans, which resulted from the transformation of $Ni(OH)_2$ and NiOOH ($Ni(OH)_2 + OH^- \leftrightarrow NiOOH + H_2O + e^-$) in alkaline electrolyte, whereas FeO_x/C did not show any observable current density in the over-potential range of <350 mV.[44,45] However, it should be mentioned that Fe oxide also has redox peaks at potentials of between −1.2 and −0.6 V (vs MMO) in alkaline electrolyte, which is out of the overpotential range studied.[46,47]

For Ni−Fe bimetallic catalysts, the $Ni(OH)_2$/NiOOH redox peaks were positively shifted with increasing Fe composition, while the redox peaks area decreased simultaneously.[30,31,33,36] When the Fe composition was greater than 54%, the electrochemical oxidation and reduction peaks became less pronounced, and the oxidation peak was even overlapped with the rapidly increased OER current. The addition of Fe may suppress the electrochemical oxidation of $Ni(OH)_2$ to NiOOH, and the number of electrons transferred per Ni atom could also be changed.[34] In order to reveal the effect of Fe content on the OER activity of Ni−Fe catalysts, the reduction peak position as a function of Fe content was plotted, as shown in Figure 3b. A linear correlation between the position of the reduction peak and Fe content is obtained, where a higher incorporated Fe content gives rise to a more positive shift of the reduction peak. However, the OER activity of the Ni−Fe catalysts is not monotonically enhanced with increasing Fe content. $Ni_{0.69}Fe_{0.31}O_x$/C, which is examined with the optimal Fe content, exhibited the highest OER activity with a 280 mV overpotential at 10 mA cm^{-2} in 1.0 M KOH, compared to the 335 mV overpotential observed on the monometallic NiO_x/C catalyst. The significant enhancement of the OER activity indicates that Fe involved in the amorphous Ni−Fe catalyst interacts closely with Ni. When the Fe content was further increased, the OER activity of Ni−Fe catalysts decreased. For instance, the OER overpotential on $Ni_{0.25}Fe_{0.75}O_x$/C at 10 mA cm^{-2} increased to 341 mV, which is close to the 335 mV overpotential of monometallic NiO_x/C. This activity drop is probably ascribed to the decrease in the number of Ni active sites on the catalyst surface with the addition of more Fe. However, due to the complex amorphous structure of Ni−Fe catalysts, the mechanisms of OER activity varying with Fe content still needs to be further investigated. It should be mentioned that the optimal Fe content varies from 10 to 50% for different Ni−Fe OER catalysts, as reported in previous publications. This may be due to different catalyst morphology and structure (crystallization vs amorphous) resulting from synthesis methods and electrode preparation techniques.[15−20] In addition, the 280 mV overpotential on the $Ni_{0.69}Fe_{0.31}O_x$/C catalyst at 10 mA cm^{-2} is also lower than the 305 mV overpotential on the well-known most active Ir/C, as shown in Figure 4a. Because IrO_x has been found to be unstable in basic solution in the high-current-density region, the recorded first cycle voltammogram was recorded for this comparison. Thus, the ca. 25 mV overpotential difference at 10 mA cm^{-2} between $Ni_{0.69}Fe_{0.31}O_x$/C and Ir/C indicates higher OER activity for the amorphous Ni−Fe catalysts. Moreover, in order to investigate the effect of carbon supporting material on $Ni_yFe_{1-y}O_x$/C OER activity, a blank CV test on carbon black (without metal nanoparticles) was carried out under the same experimental conditions. Interestingly, a very low current density was observed in the overpotential region of <450 mV, indicating a sluggish OER activity over the carbon black. Thus, the high

dx.doi.org/10.1021/la501246e | *Langmuir* 2014, 30, 7893−7901

OER performance achieved on the reported $Ni_yFe_{1-y}O_x$/C catalysts is contributed by Ni−Fe bimetallic nanoparticles, rather than the carbon black supporting material.

The Tafel plots for the carbon-supported Ni−Fe and Ir catalysts in alkaline media are shown in Figure 4b. The observed Tafel slope of the $Ni_{0.69}Fe_{0.31}O_x$/C catalyst was about 30 mV dec^{-1}, while those of NiO_x/C and Ir/C catalysts were 38 and 44 mV dec^{-1}, respectively. The turnover frequency (TOF) of the $Ni_{0.69}Fe_{0.31}O_x$/C catalyst at an overpotential of 300 mV was also calculated in 1.0 M KOH, assuming all of the active metal atoms in the catalysts drop-casted on the glassy carbon electrode are catalytically active for OER.[3,10,16,33,48] The TOF value of $Ni_{0.69}Fe_{0.31}O_x$/C was calculated to be 0.20 s^{-1}, which is similar to the previously reported highest TOF of 0.21 s^{-1} for the Ni−Fe thin film, and is roughly 10-fold higher than that of the reported IrO_x (0.0089 s^{-1}) catalyst, suggesting a high OER activity on amorphous Ni−Fe nanoparticles.[48] It should be noted that the porous structure of carbon supporting materials could affect the OER performance of the metal catalysts, since some of the Ni−Fe surface-active sites may not directly contact the electrolyte. Therefore, the obtained TOF of the $Ni_{0.69}Fe_{0.31}O_x$/C catalyst should be the lowest boundary and smaller than its actual TOF value. Corrigan has reported the highest Tafel slope of 25 mV dec^{-1} for the 10% Fe coprecipitated Ni−Fe thin film and has shown a measured current of 100 mA at a 287 mV overpotential in 1.0 M KOH.[30,31] On the basis of their reported data, the TOF was calculated to be 0.07 s^{-1}, which is much smaller than that of the presented carbon-supported amorphous $Ni_{0.69}Fe_{0.31}O_x$ nanoparticles. In addition, $Ba_{0.5}Sr_{0.5}Co_{0.8}Fe_{0.2}O_{3-\delta}$ (BSCF), reported by Suntivich et al., has a very high TOF of ∼0.6 s^{-1} at 300 mV in 0.1 M KOH.[25] However, the large particle size of ∼200 nm and the 50 mV dec^{-1} Tafel slope of BSCF will limit its OER mass activity enhancement, particularly at high overpotentials. The interaction effects between the Ni−Fe metal catalysts and the supporting material on the OER activity should be thoroughly investigated because the porous structure of carbon black that is currently used may not give rise to the optimum contact between the metal catalytic sites and electrolyte. Nitrogen-doped carbon nanotubes, 3D graphene, or reticulated vitreous carbon could be more promising alternative electrocatalyst supports, which are worthy of exploring in future research.

3.3.2. Faradaic Efficiency. The Faradaic efficiency of OER can be determined by RRDE, where oxygen was produced at the center disk electrode and collected and reduced on the Pt ring electrode. The background Pt ring current was measured and corrected prior to the experiments, and then the disk electrode was applied to consecutive 1 min constant potential steps from 0.586 to 0.646 V (vs MMO) at a 1600 rpm rotation rate under a N_2 gas blanket. The ring current was recorded at a constant potential of −0.6 V (vs MMO), which was sufficiently negative to reduce the collected oxygen rapidly. It should be noted that only dissolved O_2 can be reduced at the surface of the ring electrode. Hence, the measured Faradaic efficiency could be lower than the actual value due to the undissolved oxygen bubbles.[6] The Faradaic efficiency can be determined as below

$$\text{Faradaic efficiency} = \frac{n_{app} \times i_r}{i_d \times N} \quad (4)$$

where n_{app} is apparent number of electrons, i_r and i_d are the measured ring and disk currents, respectively, and N is the collection efficiency of RRDE, ∼0.23 in this work.

Under the conditions of −0.6 V vs MMO in 1.0 M KOH on the Pt ring electrode at a rotation rate of 1600 rpm, the apparent number of electrons, n_{app} is calculated as 2 (n_{app}= ca. 2), which was reported by Jaramillo et al.[6] They investigated the apparent number of electrons for oxygen reduction reaction (ORR) on a Pt ring electrode in 1.0 M KOH electrolyte and found that the limiting ring current is strongly related to the apparent number of electrons and rotation rate of the Pt ring electrode, based on the Levich equation of RRDE.[6,49]

The disk and ring currents over the $Ni_{0.69}Fe_{0.31}O_x$/C catalyst in 1.0 M KOH are plotted as a function of the applied disk potential in Figure 5. The highest Faradaic efficiency, ∼97%,

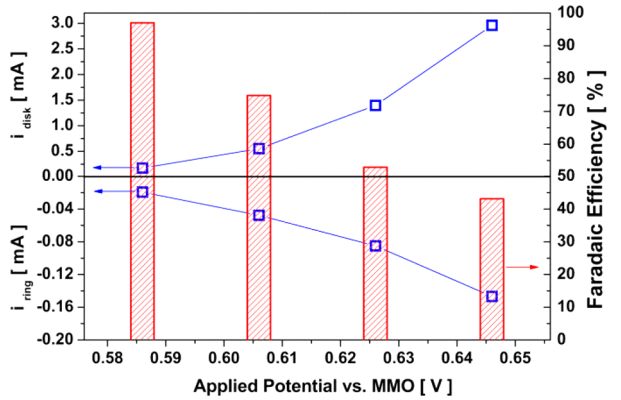

Figure 5. Faradaic efficiency measurement for the carbon-supported $Ni_{0.69}Fe_{0.31}O_x$ catalyst in 1.0 M KOH at 1600 rpm under N_2 saturation. The disk and ring currents of RRDE are plotted as functions of the applied disk potential.

was obtained at the applied disk potential of 0.586 V (vs MMO), and decreased to 43% with the disk voltage increasing to 0.646 V (vs MMO). The decreasing Faradaic efficiency might be ascribed to apparently undissolved oxygen bubbles generated at the relatively high applied disk potentials. Most of the oxygen in the gas bubble cannot be collected by the Pt ring electrode. Thus, the 97% Faradaic efficiency, achieved at 0.586 V (vs MMO) (obtained 1.0 mA cm^{-2} disk current density), is more representative of the OER efficiency on the Ni−Fe catalysts because such a disk current density is sufficiently high to generate dissolved oxygen while satisfactorily low to suppress local oxygen bubble formation at the surface of the disk electrode. The Faradaic efficiency of ∼97% suggests that the disk current is dominantly attributed to OER rather than non-OER reactions (e.g., carbon corrosion, further oxidation of nanoparticle catalyst, etc.).

3.3.3. Catalyst Stability. The short-term stability of the optimized $Ni_{0.69}Fe_{0.31}O_x$/C catalyst was investigated by chronoamperometry. A current density of 10 mA cm^{-2} was held for 6 h at a rotation rate of 1600 rpm. The cyclic voltammogram was collected after each hour to study the change in the OER activity on $Ni_{0.69}Fe_{0.31}O_x$/C, and the results are shown in Figure 6a. It is exciting to observe that after a 6 h test, the cyclic voltammograms showed no apparent change, implying that the Ni−Fe catalyst was not deactivated in 1.0 M KOH. Bell and coworkers found that the redox couple of the NiO_x thin film will shift to a higher overpotential in alkaline media after several hours of anodization, which is ascribed to

dx.doi.org/10.1021/la501246e | Langmuir 2014, 30, 7893−7901

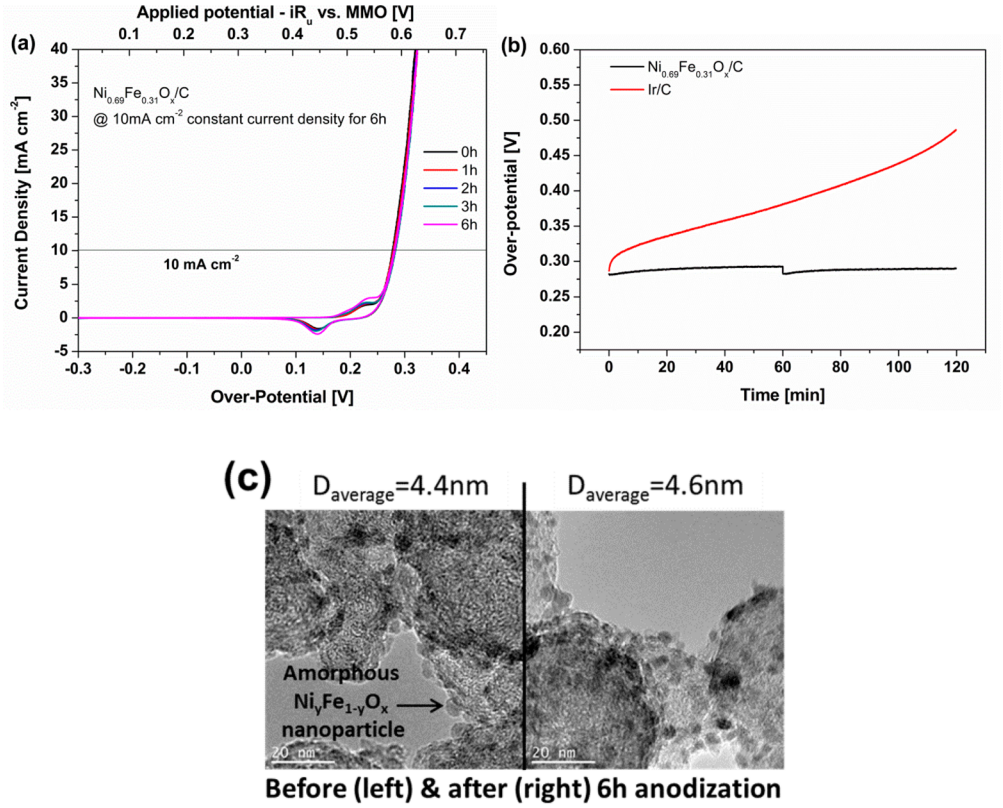

Figure 6. (a) Cyclic voltammograms of carbon-supported $Ni_{0.69}Fe_{0.31}O_x$ nanoparticles collected hourly at 5 mV s^{-1} and 1600 rpm in O_2-saturated 1.0 M KOH during 6 h of a constant current density (10 mA cm^{-2}) anodization test. (b) Plots of overpotential as a function of time for carbon-supported $Ni_{0.69}Fe_{0.31}O_x$ and Ir catalysts recorded under a 10 mA cm^{-2} constant current density at 1600 rpm in O_2-saturated 1.0 M KOH. (c) TEM images of carbon-supported $Ni_{0.69}Fe_{0.31}O_x$ before and after 6 h of a constant current density anodization test.

the transformation of disordered γ-NiOOH to ordered β-NiOOH.[33] However, the slight increase in the redox peaks area without a position shift of the redox couple is observed in the $Ni_{0.69}Fe_{0.31}O_x$/C catalyst stability tests, which could be explained as the incorporated Fe influencing the transformation of disordered γ-NiOOH to ordered β-NiOOH and more Ni surface sites exposed to electrolyte and becoming electrochemically active during the anodization.[16,33]

In order to investigate the stability of as-prepared Ni−Fe nanoparticle catalysts further, TEM was employed to reveal the nanoparticle size change before and after 6 h of anodization. Particle aggregation often occurs under high current density and has been identified as one of the main reasons leading to the decrease in catalyst activity, owing to the reduced electrochemically active surface area. However, it was interesting to observe nearly no catalyst particle aggregation after 6 h of constant current anodization, as shown in Figure 6c (TEM images for $Ni_{0.69}Fe_{0.31}O_x$/C before and after 6 h of OER testing). The average $Ni_{0.69}Fe_{0.31}O_x$ particle size measured after 6 h of OER was about 4.6 nm, which is very close to the initial value of 4.4 nm for the fresh catalyst. This negligible size change of $Ni_{0.69}Fe_{0.31}O_x$ nanoparticles further confirms the robust stability of the presented small amorphous Ni−Fe nanoparticle catalysts.

In addition, the stability of commercial Ir/C in 1.0 M KOH has also been studied for comparison with the amorphous Ni−Fe nanoparticle catalysts. Figure 6b shows the overpotential as a function of time for carbon-supported $Ni_{0.69}Fe_{0.31}O_x$ and Ir for 2 h. The Ni−Fe catalyst exhibited a surprisingly high electrochemical stability: the overpotential of the $Ni_{0.69}Fe_{0.31}O_x$ catalyst at 10 mA cm^{-2} was maintained at around 285 mV during the 2 h test. The slight increase in overpotential during the first 60 min for the Ni−Fe catalyst resulted from oxygen bubbles accumulating at the surface of the electrode. After removal of the bubbles by lifting the working electrode out of the electrolyte and rotating it, the measured OER overpotential reduced to the initial value. On the contrary, the OER overpotential on the iridium catalyst at 10 mA cm^{-2} was tremendously increased from 286 mV to 480 mV during 2 h of anodization, indicating that the Ir/C catalyst is very unstable in 1.0 M KOH. This could be explained by the oxidation of the surface IrO_x to water-soluble IrO_4^{2-} or other water-soluble solvated Ir(VI) ions, which has been reported in the literature.[50−52]

4. CONCLUSIONS

We have successfully synthesized carbon-supported amorphous Ni−Fe nanoparticle catalysts with an average size of 4 nm through a solution-phase reduction route. XRD and TEM-SAED characterizations showed that all Ni−Fe catalysts are predominantly amorphous, containing a small crystalline phase. The highest OER activity of catalysts was observed for a 31% Fe content Ni−Fe bimetallic catalyst ($Ni_{0.69}Fe_{0.31}O_x$/C) in 1.0 M KOH, which exhibited a 280 mV overpotential at 10 mA cm^{-2}. It was not only lower than the 335 mV overpotential with the amorphous NiO_x/C catalyst but also lower than the 305 mV overpotential with commercial Ir/C. The Tafel slope of 30 mV dec^{-1} with optimized $Ni_{0.69}Fe_{0.31}O_x$/C was comparable to those with the state-of-the-art Ir catalyst and Ni−Fe thin film in an alkaline electrolyte. Moreover, an attractive 97% Faradaic

dx.doi.org/10.1021/la501246e | Langmuir 2014, 30, 7893−7901

efficiency implies that the majority of the current density is attributed to the OER rather than to other side reactions. The OER overpotential remained nearly constant at around 285 mV at 10 mA cm^{-2} during 6 h of anodization. TEM images further show that the average Ni−Fe particle size apparently did not change (from 4.4 to 4.6 nm) and no obvious Ni−Fe nanoparticle aggregation was observed. All of these strongly indicate the robust stability of the small amorphous Ni−Fe nanoparticle catalyst for alkaline OER. The reported amorphous Ni−Fe nanoparticles with high OER efficiency and stability can potentially serve as electrocatalysts for (photo)electrochemical cells in water splitting or CO_2 reduction applications.

AUTHOR INFORMATION

Corresponding Author

*E-mail: wzli@mtu.edu. Fax: +1-906-487-3213. Tel: +1-906-487-2298.

Author Contributions

Y.Q. and L.X. contributed equally.

Notes

The authors declare no competing financial interest.

ACKNOWLEDGMENTS

We acknowledge partial financial support from the U.S. National Science Foundation (CBET-1235982). We also thank D. Chadderdon and J. Qi for fruitful discussions.

REFERENCES

(1) Bard, A. J.; Fox, M. A. Artificial Photosynthesis - Solar Splitting of Water to Hydrogen and Oxygen. *Acc. Chem. Res.* **1995**, *28*, 141−145.

(2) Walter, M. G.; Warren, E. L.; McKone, J. R.; Boettcher, S. W.; Mi, Q. X.; Santori, E. A.; Lewis, N. S. Solar Water Splitting Cells. *Chem. Rev.* **2010**, *110*, 6446−6473.

(3) Liang, Y.; Li, Y.; Wang, H.; Dai, H. Strongly Coupled lnorganic/Nanocarbon Hybrid Materials for Advanced Electrocatalysis. *J. Am. Chem. Soc.* **2013**, *135*, 2013−2036.

(4) Cook, T. R.; Dogutan, D. K.; Reece, S. Y.; Surendranath, Y.; Teets, T. S.; Nocera, D. G. Solar Energy Supply and Storage for the Legacy and Non legacy Worlds. *Chem. Rev.* **2010**, *110*, 6474−6502.

(5) Lewis, N. S. Toward cost-effective solar energy use. *Science* **2007**, *315*, 798−801.

(6) McCrory, C. C. L.; Jung, S.; Peters, J. C.; Jaramillo, T. F. Benchmarking Heterogeneous Electrocatalysts for the Oxygen Evolution Reaction. *J. Am. Chem. Soc.* **2013**, *135*, 16977−16987.

(7) Xin, L.; Zhang, Z. Y.; Qi, J.; Chadderdon, D. J.; Qiu, Y.; Warsko, K. M.; Li, W. Z. Electricity Storage in Biofuels: Selective Electrocatalytic Reduction of Levulinic Acid to Valeric Acid or gamma-Valerolactone. *ChemSusChem* **2013**, *6*, 674−686.

(8) Qiu, Y.; Xin, L.; Chadderdon, D. J.; Qi, J.; Liang, C.; Li, W. Z. Integrated electrocatalytic processing of levulinic acid and formic acid to produce biofuel intermediate valeric acid. *Green Chem.* **2014**, *16*, 1305−1315.

(9) Koper, M. T. M. Thermodynamic theory of multi-electron transfer reactions: Implications for electrocatalysis. *J. Electroanal. Chem.* **2011**, *660*, 254−260.

(10) Kanan, M. W.; Nocera, D. G. In situ formation of an oxygen-evolving catalyst in neutral water containing phosphate and Co^{2+}. *Science* **2008**, *321*, 1072−1075.

(11) Dau, H.; Limberg, C.; Reier, T.; Risch, M.; Roggan, S.; Strasser, P. The Mechanism of Water Oxidation: From Electrolysis via Homogeneous to Biological Catalysis. *ChemCatChem* **2010**, *2*, 724−761.

(12) Gorlin, Y.; Jaramillo, T. F. Investigation of Surface Oxidation Processes on Manganese Oxide Electrocatalysts Using Electrochemical Methods and Ex Situ X-ray Photoelectron Spectroscopy. *J. Electrochem. Soc.* **2012**, *159*, H782−H786.

(13) Man, I. C.; Su, H.-Y.; Calle-Vallejo, F.; Hansen, H. A.; Martínez, J. I.; Inoglu, N. G.; Kitchin, J.; Jaramillo, T. F.; Nørskov, J. K.; Rossmeisl, J. Universality in Oxygen Evolution Electrocatalysis on Oxide Surfaces. *ChemCatChem* **2011**, *3*, 1159−1165.

(14) Lee, Y.; Suntivich, J.; May, K. J.; Perry, E. E.; Shao-Horn, Y. Synthesis and Activities of Rutile IrO_2 and RuO_2 Nanoparticles for Oxygen Evolution in Acid and Alkaline Solutions. *J. Phys. Chem. Lett.* **2012**, *3*, 399−404.

(15) Chou, N. H.; Ross, P. N.; Bell, A. T.; Tilley, T. D. Comparison of Cobalt-based Nanoparticles as Electrocatalysts for Water Oxidation. *ChemSusChem* **2011**, *4*, 1566−1569.

(16) Esswein, A. J.; McMurdo, M. J.; Ross, P. N.; Bell, A. T.; Tilley, T. D. Size-Dependent Activity of Co_3O_4 Nanoparticle Anodes for Alkaline Water Electrolysis. *J. Phys. Chem. C* **2009**, *113*, 15068−15072.

(17) Pickrahn, K. L.; Park, S. W.; Gorlin, Y.; Lee, H.-B.-R.; Jaramillo, T. F.; Bent, S. F. Active MnO_x Electrocatalysts Prepared by Atomic Layer Deposition for Oxygen Evolution and Oxygen Reduction Reactions. *Adv. Energy Mater.* **2012**, *2*, 1269−1277.

(18) Gorlin, Y.; Jaramillo, T. F. A Bifunctional Nonprecious Metal Catalyst for Oxygen Reduction and Water Oxidation. *J. Am. Chem. Soc.* **2010**, *132*, 13612−13614.

(19) Liang, Y.; Li, Y.; Wang, H.; Zhou, J.; Wang, J.; Regier, T.; Dai, H. Co_3O_4 nanocrystals on graphene as a synergistic catalyst for oxygen reduction reaction. *Nat. Mater.* **2011**, *10*, 780−786.

(20) Liu, Y.; Higgins, D. C.; Wu, J.; Fowler, M.; Chen, Z. Cubic spinel cobalt oxide/multi-walled carbon nanotube composites as an efficient bifunctionalelectrocatalyst for oxygen reaction. *Electrochem. Commun.* **2013**, *34*, 125−129.

(21) Man, I. C.; Su, H. Y.; Calle-Vallejo, F.; Hansen, H. A.; Martinez, J. I.; Inoglu, N. G.; Kitchin, J.; Jaramillo, T. F.; Norskov, J. K.; Rossmeisl, J. Universality in Oxygen Evolution Electrocatalysis on Oxide Surfaces. *ChemCatChem* **2011**, *3*, 1159−1165.

(22) Li, Y.; Hasin, P.; Wu, Y. $Ni_xCo_{3-x}O_4$ Nanowire Arrays for Electrocatalytic Oxygen Evolution. *Adv. Mater.* **2010**, *22*, 1926−1929.

(23) Bockris, J. O.; Otagawa, T. Mechanism of Oxygen Evolution on Perovskites. *J. Phys. Chem.* **1983**, *87*, 2960−2971.

(24) Bockris, J. O.; Otagawa, T. The Electrocatalysis of Oxygen Evolution on Perovskites. *J. Electrochem. Soc.* **1984**, *131*, 290−302.

(25) Suntivich, J.; May, K. J.; Gasteiger, H. A.; Goodenough, J. B.; Shao-Horn, Y. A Perovskite Oxide Optimized for Oxygen Evolution Catalysis from Molecular Orbital Principles. *Science* **2011**, *334*, 1383−1385.

(26) Landon, J.; Demeter, E.; Inoglu, N.; Keturakis, C.; Wachs, I. E.; Vasic, R.; Frenkel, A. I.; Kitchin, J. R. Spectroscopic Characterization of Mixed Fe-Ni Oxide Electrocatalysts for the Oxygen Evolution Reaction in Alkaline Electrolytes. *ACS Catal.* **2012**, *2*, 1793−1801.

(27) Li, X. H.; Walsh, F. C.; Pletcher, D. Nickel based electrocatalysts for oxygen evolution in high current density, alkaline water electrolysers. *Phys. Chem. Chem. Phys.* **2011**, *13*, 1162−1167.

(28) Potvin, E.; Brossard, L. Electrocatalytic activity of Ni-Fe anodes for alkaline water electrolysis. *Mater. Chem. Phys.* **1992**, *31*, 311−318.

(29) Gong, M.; Li, Y.; Wang, H.; Liang, Y.; Wu, J. Z.; Zhou, J.; Wang, J.; Regier, T.; Wei, F.; Dai, H. An Advanced Ni-Fe Layered Double Hydroxide Electrocatalyst for Water Oxidation. *J. Am. Chem. Soc.* **2013**, *135*, 8452−8455.

(30) Corrigan, D. A. The Catalysis of the Oxygen Evolution Reaction by Iron Impurities in Thin-Film Nickel-Oxide Electrodes. *J. Electrochem. Soc.* **1987**, *134*, 377−384.

(31) Corrigan, D. A.; Bendert, R. M. Effect of Coprecipitated Metal-Ions on the Electrochemistry of Nickel-Hydroxide Thin-Films - Cyclic Voltammetry in 1m Koh. *J. Electrochem. Soc.* **1989**, *136*, 723−728.

(32) Grosso, D.; Cagnol, F.; Soler-Illia, G. J. D. A.; Crepaldi, E. L.; Amenitsch, H.; Brunet-Bruneau, A.; Bourgeois, A.; Sanchez, C. Fundamentals of mesostructuring through evaporation-induced self-assembly. *Adv. Funct. Mater.* **2004**, *14*, 309−322.

(33) Louie, M. W.; Bell, A. T. An Investigation of Thin-Film Ni-Fe Oxide Catalysts for the Electrochemical Evolution of Oxygen. *J. Am. Chem. Soc.* **2013**, *135*, 12329−12337.
(34) Yeo, B. S.; Bell, A. T. Enhanced Activity of Gold-Supported Cobalt Oxide for the Electrochemical Evolution of Oxygen. *J. Am. Chem. Soc.* **2011**, *133*, 5587−5593.
(35) Zhang, Z. Y.; Xin, L.; Qi, J.; Chadderdon, D. J.; Li, W. Z. Supported Pt, Pd and Au nanoparticle anode catalysts for anion-exchange membrane fuel cells with glycerol and crude glycerol fuels. *Appl. Catal. B* **2013**, *136*, 29−39.
(36) Zhang, Z. Y.; Xin, L.; Sun, K.; Li, W. Z. Pd-Ni electrocatalysts for efficient ethanol oxidation reaction in alkaline electrolyte. *Int. J. Hydrogen Energy* **2011**, *36*, 12686−12697.
(37) Yano, H.; Kataoka, M.; Yamashita, H.; Uchida, H.; Watanabe, M. Oxygen reduction activity of carbon-supported Pt-M (M = V, Ni, Cr, Co, and Fe) alloys prepared by nanocapsule method. *Langmuir* **2007**, *23*, 6438−6445.
(38) Paulus, U. A.; Schmidt, T. J.; Gasteiger, H. A.; Behm, R. J. Oxygen reduction on a high-surface area Pt/Vulcan carbon catalyst: a thin-film rotating ring-disk electrode study. *J. Electroanal. Chem.* **2001**, *495*, 134−145.
(39) Medway, S.L.; Lucas, C.A.; Kowal, A.; Nichols, R.J.; Johnson, D. In situ studies of the oxidation of nickel electrodes in alkaline solution. *J. Electroanal. Chem.* **2006**, *587*, 172−181.
(40) Cheng, W.; Tang, K. B.; Qi, Y. X.; Sheng, J.; Liu, Z. P. One-step synthesis of superparamagnetic monodisperse porous Fe_3O_4 hollow and core-shell spheres. *J. Mater. Chem.* **2010**, *20*, 1799−1805.
(41) Chemelewski, W. D.; Lee, H.-C.; L, J.-F.; Bard, A. J.; Buddie Mullins, C. Amorphous FeOOH Oxygen Evolution Reaction Catalyst for Photoelectrochemical Water Splitting. *J. Am. Chem. Soc.* **2014**, *136*, 2843−2850.
(42) Smith, R. D. L.; Prevot, M. S.; Fagan, R. D.; Zhang, Z. P.; Sedach, P. A.; Siu, M. K. J.; Trudel, S.; Berlinguette, C. P. Photochemical Route for Accessing Amorphous Metal Oxide Materials for Water Oxidation Catalysis. *Science* **2013**, *340*, 60−63.
(43) Dickinson, M.; Scott, T. B.; Crane, R. A.; Riba, O.; Barnes, R. J.; Hughes, G. M. The effects of vacuum annealing on the structure and surface chemistry of iron:nickel alloy nanoparticles. *J. Nanopart. Res.* **2010**, *12*, 2081−2092.
(44) Kostecki, R.; McLarnon, F. Electrochemical and in situ Raman spectroscopic characterization of nickel hydroxide electrodes. *J. Electrochem. Soc.* **1997**, *144*, 485−493.
(45) Lyons, M. E. G.; Brandon, M. P. The Oxygen Evolution Reaction on Passive Oxide Covered Transition Metal Electrodes in Aqueous Alkaline Solution. Part 1-Nickel. *Int. J. Electrochem. Soc.* **2008**, *3*, 1386−1424.
(46) Lyons, M. E. G.; Brandon, M. P. The Oxygen Evolution Reaction on Passive Oxide Covered Transition Metal Electrodes in Alkaline Solution. Part III - Iron. *Int. J. Electrochem. Soc.* **2008**, *3*, 1463−1503.
(47) Singh, R. N.; Pandey, J. P.; Anitha, K. L. Preparation of Electrodeposited Thin-Films of Nickel Iron-Alloys on Mild-Steel for Alkaline Water Electrolysis.1. Studies on Oxygen Evolution. *Int. J. Hydrogen Energy* **1993**, *18*, 467−473.
(48) Trotochaud, L.; Ranney, J. K.; Williams, K. N.; Boettcher, S. W. Solution-Cast Metal Oxide Thin Film Electrocatalysts for Oxygen Evolution. *J. Am. Chem. Soc.* **2012**, *134*, 17253−17261.
(49) Bard, A. J.; Faulkner, L. R. In *Electrochemical Methods: Fundamentals and Applications*, 2nd ed.; Wiley: New York, 2001.
(50) Minguzzi, A.; Fan, F. R. F.; Vertova, A.; Rondinini, S.; Bard, A. J. Dynamic potential-pH diagrams application to electrocatalysts for water oxidation. *Chem. Sci.* **2012**, *3*, 217−229.
(51) Guerrini, E.; Chen, H.; Trasatti, S. Oxygen evolution on aged IrO_x/Ti electrodes in alkaline solutions. *J. Solid State Electrochem.* **2007**, *11*, 939−945.
(52) Pourbaix, M. In *Atlas of Electrochemical Equilibria in Aqueous Solution*; Pergamon Press: Oxford, U.K., 1966.